nature communications

Article

https://doi.org/10.1038/s41467-025-62184-0

High strength and plasticity in disordered multilayer graphene reinforced copper composites

Received: 9 November 2024

Accepted: 11 July 2025

Published online: 23 July 2025

Check for updates

Yongfeng Geng[1], Xiaohui Zhang[1], Yufan Zheng[2], Lei Zhao[1], Zan Li[1], Xu Li[3], Ruijuan Qi[2], Zhiping Wang[4], Gang Sha[4], Di Zhang[1] & Ding-Bang Xiong[1]

Nanocrystalline (nc) metals typically possess high strength but low ductility. Here, we report an interface nanostructuring design via plasma assisted ball milling (PABM) to fabricate disordered multilayer graphene (DMGr)/Cu composites that are ultra-strong yet plastic, achieving a compressive strength of 1.56 GPa and plastic strain of exceeding 0.6. Our strategy relies on the uniformly and densely dispersed DMGr with sp^2-sp^3 hybridization. Interlayer sliding of DMGr but much stronger than van der Waals forces which can be anticipated to mediate plastic deformation and improve the plasticity. The high intrinsic strength of DMGr and associated Cu lattice strain near the interface due to strong interactions between DMGr and matrix can significantly impede dislocation motion and promote dislocation accumulation within nanograin interior. Ex-situ and in-situ TEM characterizations revealed that substantial dislocation interactions and accumulations induced by DMGr and the associated lattice strain along with interlayer sliding of DMGr, led to high strength, enhanced strain hardening capacity and superior plasticity. Such a design strategy provides a pathway for mitigating the trade-off between strength and plasticity in nanograined metals.

Nanocrystalline (nc) metals generally possess high strength but low ductility, which poses a bottleneck that limits their applications in many advanced technologies[1–3]. The trade-off between strength and ductility is a long-standing dilemma in materials science and engineering, while the improvement of both strength and ductility is highly challenging[4–7]. In NC metals, dislocations that traverse the nanograins to sustain plastic flow tend to be rapidly absorbed into the opposing grain boundaries (GBs), leaving little dislocation build-up behind[2,8,9]. Such a phenomenon in the presence of abundant GBs takes away the most prolific conventional mechanisms for strain hardening[10]. Efficient storage of dislocations in nanograins is believed to be responsible for the high strain hardening and ductility[1,3,10]. Therefore, the key to solving the low ductility problem of NC metals lies in the improvement of their strain-hardening ability, which fundamentally depends on the promoted dislocation emission and intensive dislocation accumulation within the grain interior[11–15].

Various strategies have been proposed to address the aforementioned challenges in NC metals with some success to recover the strain-hardening capability. In terms of nano-structural design, the prepared heterogeneous nanostructures, such as bimodal, harmonic, lamellar, gradient, domain-dispersed, and hierarchical nanostructures, can endow metals and alloys with superior combinations of strength and ductility that are not accessible to their homogeneous counterparts[2,16,17]. Geometrically necessary dislocations (GNDs) are generated to accommodate deformation incompatibility near heterogeneous interfaces during straining, which consequently produce

[1]State Key Lab of Metal Matrix Composites, Shanghai Jiao Tong University, Shanghai, China. [2]Key Laboratory of Polar Materials and Devices (MOE), School of Physics and Electronic Science, East China Normal University, Shanghai, China. [3]Center for Advanced Measurement Science, National Institute of Metrology, Beijing, China. [4]School of Materials Science and Engineering, Herbert Gleiter Institute of Nanoscience, Nanjing University of Science and Technology, Nanjing, China. e-mail: xiongdingbang@sjtu.edu.cn

back stress in the soft domains and forward stress in the hard domains[18]. The interactions between back stress and forward stress contribute to hetero-deformation induced (HDI) strengthening and HDI strain hardening, thus enhancing the yield strength and helping to improve the ductility[2].

Grain interior and interface engineering are also employed to surmount the dilemma. One strategy is introducing nano twins in NC metals, including gradient nanotwinned structures[19] and hierarchical nanotwinned structures[20,21], which can effectively act as barriers and accumulation sites for gliding dislocations, generate high strain hardening and hence simultaneously improve strength and ductility[5,22,23]. Another approach is employing the distribution of nano-precipitates/second-phase particles in the nanograin interior to promote the dislocation trapping, which could help sustain high work hardening and ductility[11,24,25]. By manipulating the interface nanostructuring, such as GBs segregation[26] and GBs engineering[27], their composites have the potential to simultaneously achieve high strength and high ductility. GBs segregation of solute atoms can help to impede GBs migration and relax local stress, stabilizing the nanostructures and suppressing the GBs cracking[28,29]. By embedded nanograins in an amorphous framework, dual-phase nanostructured materials possess high strength via constrained deformation confined by the boron boundary[30] or blocking the propagation of shear bands[31].

Some studies have achieved macroscopic superior mechanical properties through graphene (Gr)/Cu interface engineering. The number of Gr layers is one of the important factors affecting the properties of metal matrix composites (MMCs). Ultra-high strength of nanolayered composite with alternating layers of copper and monolayer Gr was achieved due to the significant role of monolayer Gr in blocking dislocation propagation across the interface[32]. Interlayer sliding of multilayer Gr takes place due to the van der Waals force between interlayers during plastic deformation, where high strength and formability is attained owing to the well-known Hall-Petch relation and uniformly dispersed nanoscale inter-/intra-granular Gr[33]. As the thickness of Gr at the interface further increases, the strengthening effects of multilayer Gr are deteriorated due to the weak van der Waals bonding between them in Gr/Cu dual nanophase composites, exhibiting extremely low ductility[34]. As is well known, the different mechanical behaviors of carbon materials stem from the differences in their atomic structures, such as *sp*, sp^2, and sp^3 hybridization, which provide versatility for tuning their mechanical properties in a wide range. Carbon materials with various sp^2-sp^3 mixtures have been fabricated by deposition techniques and pressure-induced phase transition of sp^2 carbon[35,36], which suggests that the presence of sp^3 covalent bonding at the interlayer of sp^2 can improve the hardness and strength of composites, avoiding premature failure caused by weak van der Waals forces. Recent work in situ synthesized C/C composites with ultra-high mechanical properties, consisting of ultrafine nanodiamond homogeneously embedded in disordered multilayer Gr (DMGr) with sp^2-sp^3 hybridization[37].

In this work, we developed an interface nanostructuring strategy to fabricate high-performance DMGr/Cu NC composites via plasma-assisted ball milling (PABM), where uniform distribution of high-density DMGr with sp^2-sp^3 hybridization was achieved. On one hand, the presence of a small amount sp^3 covalent bonding at the interlayer makes these DMGr can assist plastic deformation through interlayer sliding, but much stronger than van der Waals forces, being believed to act like a GBs sliding mechanism. On the other hand, these DMGr have high intrinsic strength, which can effectively block dislocation motions. Moreover, the strong interactions between DMGr and matrix induce lattice expansion and associated lattice strain, promoting the interactions and storage of dislocations within nanograins. Contrary to the characteristics of high strength and low ductility in NC metals, our DMGr/Cu composite presents ultra-high strength and superior plasticity with a high nanoindentation hardness of 6.2 GPa and a compressive strength of 1.56 GPa as well as a plastic strain of over 0.6 via multiple strengthening mechanisms generated by the unusual behavior of dislocation interactions and accumulations inside nanograins induced by DMGr and lattice strain and the interlayer sliding of DMGr. These results open an avenue for developing high-performance NC metals via interface nanostructuring design.

Results

Observed lattice expansion and microstructure characterizations

The DMGr/Cu composites exhibit distinct morphologies (Supplementary Figs. 1–3) and X-ray diffraction (XRD) patterns (Supplementary Figs. 6, 7), where a significant leftward shift in diffraction peaks is observed with increasing of milling time and volume fraction of DMGr. Three-dimensional distribution of lattice parameters calculated from the well-known Scherrer's equation is depicted in Fig. 1a and Supplementary Table. 2. When DMGr content is low, the lattice expansion is unstable in energy due to the fact that of inevitable temperature changes during PABM, which could lead to changes in the solubility of C in copper, ie. the formation and dissociation of the sub-solid solution, and dynamic changes of lattice expansion especially under low volume fraction of DMGr[38,39]. And lattice parameters show a fluctuating trend with the extension of milling time (Supplementary Fig. 7a), such as 0.3644 nm for 30 h and 0.3620 nm for 45 h. Nevertheless, with the concentration of DMGr exceeding 5 vol%, the diffraction peaks constantly shift to a lower angle with the extension of milling time (Supplementary Fig. 7e), and the lattice parameter reaches the maximum value of 0.3670 nm for 80 h.

Furtherly, we characterized 1.5 vol% DMGr/Cu composite milling for 30 h (denoted as 1.5 vol% DMGr/Cu-30 h) by combining Scanning Transmission Electron Microscopy (STEM) and advanced characterization techniques. The NC-composite exhibits an average grain size of 75 nm and uniform distribution of DMGr (9.7 nm), as revealed by the STEM images (Supplementary Fig. 8). We adopted the integrated differential phase-contrast scanning transmission electron microscopy (iDPC-STEM) technique to characterize the structure of the composite, which can simultaneously achieve high-resolution imaging of light and heavy atoms[40]. Figure 1d shows the atomic configuration of containing DMGr region in an enlargement of high-angle annular dark-field (HAADF) image (Fig. 1c) with the incident electron beam aligned along $[1\bar{1}0]$ the zone axis. A significant increment of interplanar spacing is observed in the region near the DMGr/Cu interface: 0.2154 nm for (111) and 0.2162 nm for $(11\bar{1})$ the plane, respectively (Fig. 1e). Moreover, the interplanar spacing away from the DMGr region is also higher than the theoretical value of (111) the plane. Meanwhile, lattice expansion causes Cu atoms to deviate from their equilibrium position and could result in lattice strain. We used geometric phase analysis (GPA) methods[41] based on atomic morphology to characterize the lattice strain in the composite. As displayed by the GPA atomic strain maps along ε_{xx} and ε_{xy} (Supplementary Fig. 9), the strain distribution is relatively random with the trend of fluctuations, suggesting the presence of lattice strain near the DMGr/Cu interfaces, which can result in stronger resistance to dislocation motion. Correspondingly, the lattice strain in the region of away from DMGr is significantly lower, consistent with the results of interplanar spacing.

Figure 1g shows the electron energy loss near edge structure (ELNES) of the C-K edge at different regions of DMGr, DMGr-Cu interface, and matrix away from DMGr, where two energy loss peaks can be observed in both regions of DMGr and DMGr-Cu interface ($1s \rightarrow \pi^*$ transition peak at ~285 eV and $1s \rightarrow \sigma^*$ transition peak at ~ 294 eV)[11,42], indicating the presence of C element near the interface. In addition to the observed peaks of C 1*s*-π^*/σ^*, two additional significant peaks are also observed, including an adsorption peak of C-O bond (~ 288 eV) from residual functional groups in RGO and an adsorption peak (~ 292 eV) of sp^3 bonding[43], which can be also observed in X-ray

https://doi.org/10.1038/s41467-025-62184-0

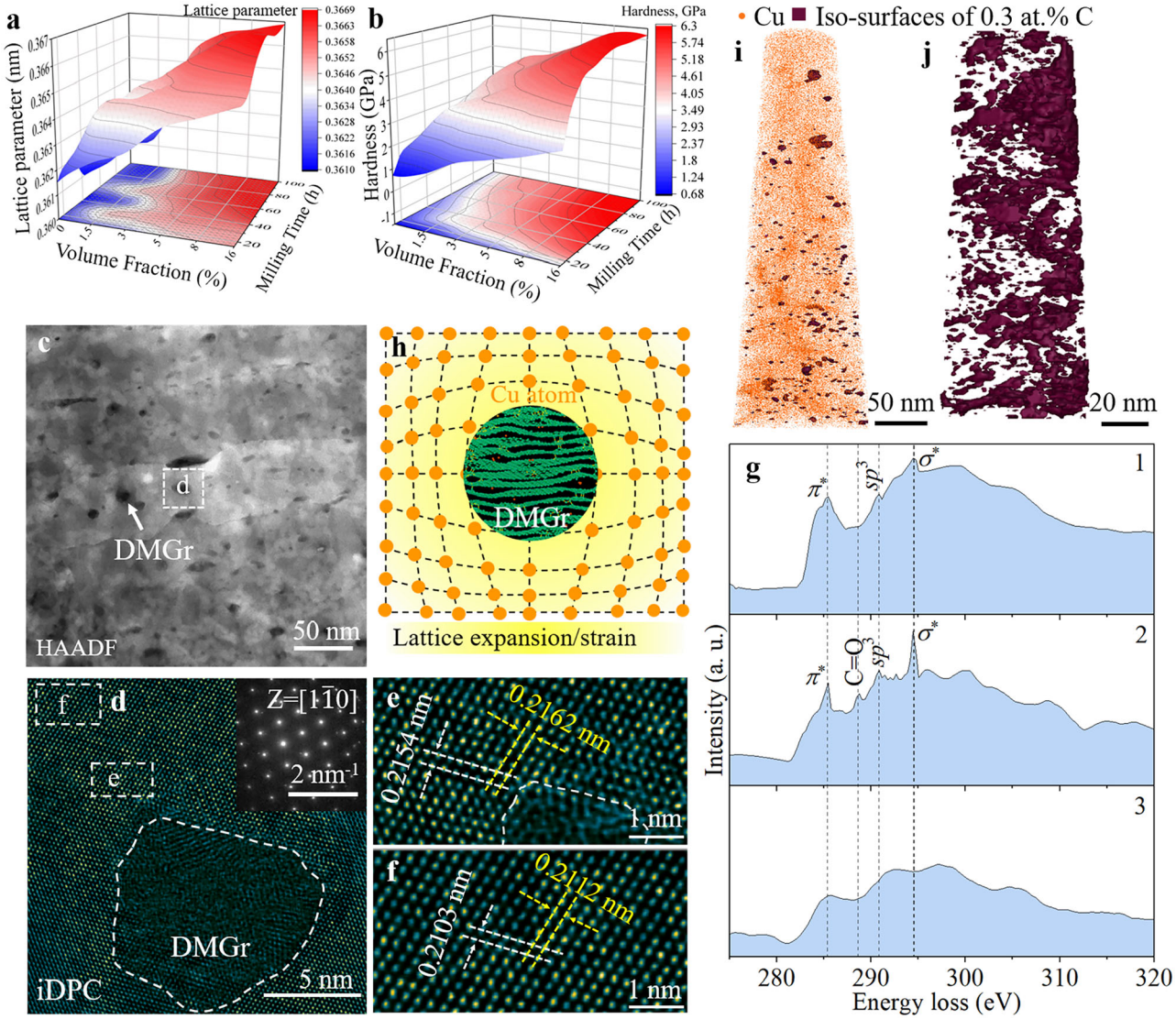

Fig. 1 | Lattice parameters, hardness, microstructure and thermal stability of disordered multilayer graphene (DMGr)/Cu composites. Three-dimensional distribution of lattice parameters (**a**) and nanoindentation results (**b**) for DMGr/Cu composites with different volume milling for different times. **c**–**i** Microstructure characterizations of 1.5 vol% DMGr/Cu-30 h. **c** High-angle annular dark-field scanning transmission electron microscopy (HAADF-STEM) image showing uniform distribution of DMGr. **d** Integrated differential phase-contrast (iDPC) image marked by b in (**a**) taken with [1$\bar{1}$0] zone axis, showing the atomic structure. The red dashed line represents a DMGr particle with a characteristic of disordered atomic structure. **e** Enlargement of iDPC image in (**b**) marked by e near DMGr. **f** Enlargement of iDPC image in (**b**) marked by f far away from DMGr. **g** Electron energy loss near edge structure (ELNES) spectrum at the C-K edge for different regions, including DMGr (1), DMGr-Cu interface (2), and matrix away from DMGr (3). **h** Schematic map of lattice expansion and lattice strain caused by DMGr, and the magnification of DMGr is presented in Supplementary Fig. 11. **i** Cu atom map of a reconstructed volume of 1.5 vol% DMGr/Cu-30 h sample with iso-surfaces at 0.3 at. % C. **j** A reconstructed volume of a 16 vol% DMGr/Cu-60 h sample, with iso-surfaces (in black red) at 0.3 at. % C.

photoelectron spectroscopy (XPS, Supplementary Fig. 4). Therefore, the DMGr in our composites are a class of mixed sp^2-sp^3 hybridized carbons with a low sp^3 component, presence of which make the interlayer force of DMGr much stronger than van der Waals force between multilayer Gr. But these peaks disappear in the matrix away from DMGr (>1 nm). Furthermore, from the interface to the DMGr domain, there is a drop in intensity of the π^* peak, i.e., a lower fraction of the sp^2 signal peak, indicating an increase of sp^3 bonding in the DMGr region[36,37]. The increased I_D/I_G intensity ratios is observed with extended milling time, suggesting an increased fraction of sp^3 bonding (Supplementary Fig. 5)[44].

We further conducted atom probe tomography (APT) experiments to characterize the C element distribution. The side-view APT images of 1.5 vol% DMGr/Cu-30 h and 16 vol% DMGr/Cu-60 h (Fig. 1i, j, and Supplementary Fig. 10) show the uniform distribution of the C element. The typical proxigrams of selected DMGr reveal that C element concentration is a gradient in the region from − 4 nm to 0 nm, which suggests that C element only enters the Cu lattice near the interface, consistent with the electron energy loss spectra (EELS) analysis. Consequently, our analysis further confirms the inference in refs. 38,39, but the C atoms can only enter the Cu lattice near the interface. Density functional theory (DFT) calculations indicate that short-circuit diffusion of C atoms and formation of Cu-C bonding jointly contribute to dissolution of C atoms in Cu lattice under the drive of lattice distortion energy generated by high-density lattice defects (Supplementary Note 1). In addition, the solid solution carbon atom and interface stress induced by high-density defects of DMGr, i.e., the strong interactions between DMGr and Cu, are the main

https://doi.org/10.1038/s41467-025-62184-0

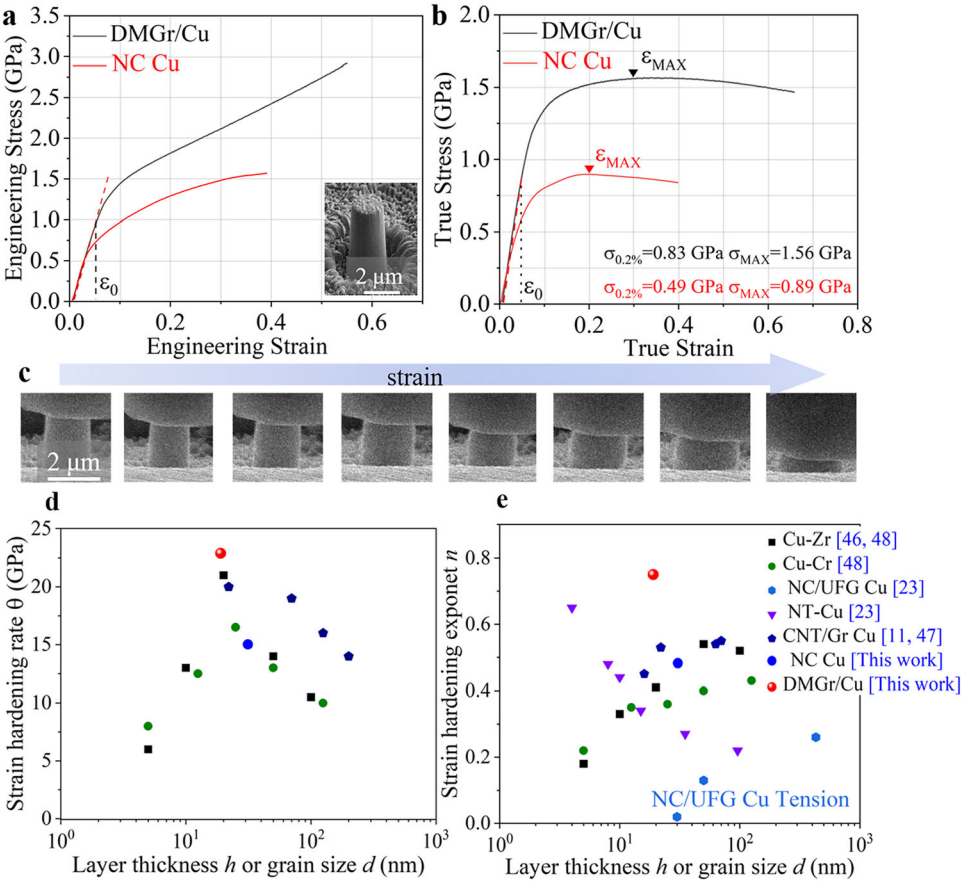

Fig. 2 | Mechanical properties of nanocrystalline (NC) Cu and 16 vol% DMGr/Cu-60 h. a Engineering stress-strain curves, the inset represents scanning electron microscope (SEM) morphology of the micropillar. **b** True stress-strain curves. **c** Snaps of the micropillar deformed at different strains. **d** Strain hardening rate Θ as a function of layer thickness (h) or grain size (d). **e** Strain hardening exponent n as a function of h or d. Here, the data of carbon nanotubes (CNTs)/Gr Cu, Cu-Cr, and Cu-Zr were obtained from the micropillar compression[32,46–48], while Gr/Cu[11], nanotwin (NT)-Cu, NC Cu, and ultrafine-grains (UFG) Cu[23] came from the uniaxial tension.

reasons that bring about lattice expansion/strain (Supplementary Note 2). The schematic map showing lattice expansion/strain is displayed in Fig. 1h.

Mechanical properties

Nanoindentation tests were performed on the synthesized DMCr/Cu composites to obtain their hardness values according to the continuous stiffness method (CSM). Representative loading-unloading curves and corresponding nanoindentation marks are presented in Supplementary Fig. 12a. The results of nanoindentation revealed that the hardness value continuously increased with the increasing of DMGr volume fraction and ball milling time (Fig. 1b and Supplementary Table. 2). Furthermore, the 16 vol% DMGr/Cu-60 h exhibited the maximum values of 6.16 ± 0.54 GPa, exceeding these values reported in other Cu matrix composites, including Gr/Cu, carbon nanotubes (CNTs)/Cu, Cu-B, Cu-Al, Cu-W, Cu-Zr and Cu-Cr measured in terms of volume fraction (Supplementary Fig. 12b). Therefore, the sample of 16 vol% DMGr/Cu-60 h was selected to carry out the micropillar compression test in order to investigate its deformation behavior and obtain corresponding compressive strength (Supplementary Movie 1). The morphology of a micropillar with a diameter of 2 μm is exhibited in the inset of Fig. 2a. The engineering stress-strain curve during compression is exceedingly smooth without any pop-in points (Fig. 2a). And the true stress-true strain curve derived from the engineering stress-strain curve (Fig. 2b) shows a yield strength of 0.83 GPa, flow stress of 1.56 GPa, and plastic strain of exceeding 0.6. Moreover, snaps of the 16 vol% DMGr/Cu-60 h sample at progressive strain was displayed in Fig. 2c, indicating high plasticity. While the yield strength and flow stress of NC Cu without DMGr addition under the same milling time are only 0.49 GPa and 0.89 GPa, respectively. The yield strength of NC Cu in this work exhibits equivalent values compared with conventional NC Cu under a similar grain size[45]. Based on the true stress-strain curve and strain hardening rate curve, we calculated the strain hardening rate and strain hardening exponent of our composite. Strain hardening rate (θ) value were calculated to be 22.9 GPa for DMGr/Cu and 15.1 GPa for NC Cu, respectively, at strain of 0.04 by using the strain hardening rate (Supplementary Fig. 13a), ie., $\theta = d\sigma/d\varepsilon$ [11]. And strain hardening exponent (n) was determined to be 0.75 for DMGr/Cu and 0.48 for NC Cu at strain of 0.04, respectively, by fitting the uniform plastic deformation region to $\sigma = K_1 + K_2\varepsilon_p^n$ (Supplementary Fig. 13b)[23], where K_1 denotes the initial yield strength, K_2 represents the strengthening coefficient, and n is the strain hardening exponent. Our composite exhibits the maximum values of θ (Fig. 2d) and n (Fig. 2e) compared with other Cu matrix composites, ultrafine-grain (UFG) Cu, and NC Cu, suggesting superior strain hardening capacity[11,23,32,46–48]. The calculated strain hardening exponent in uniaxial tension of Gr/Cu prepared by high-energy ball milling is only 0.54[11]. It should be noted that the strain hardening rate and strain hardening exponent of DMGr/Cu composite are much higher than that of NC Cu under the same milling time, which proves the significant importance of our uniformly and densely dispersed DMGr and associated lattice strain in achieving high strength and superior plasticity.

https://doi.org/10.1038/s41467-025-62184-0

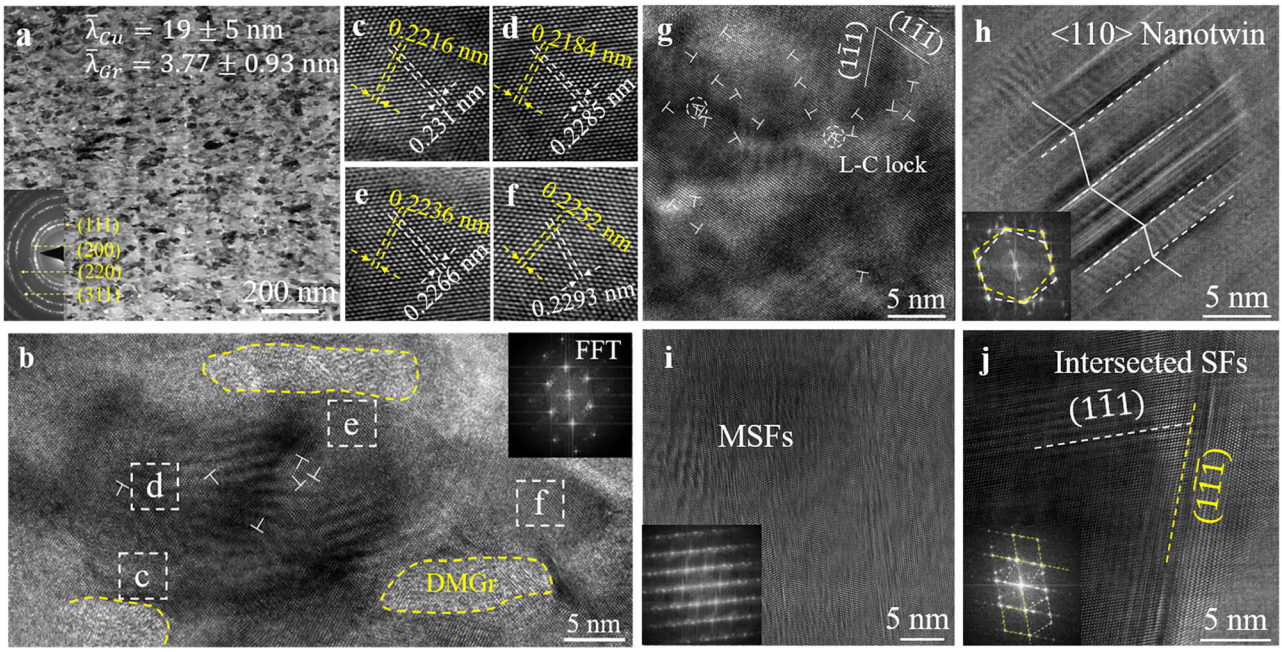

Fig. 3 | Microstructure of 16 vol% DMGr/Cu-60 h before (a–f) and after micropillar compression (g–j). a Bright field scanning transmission electron microscopy (BF-STEM) image. The inset shows the selected-area electron diffraction (SAED) pattern. **b** High-resolution transmission electron microscopy (HRTEM) image showing DMGr along grain boundaries (GBs) taken with [1$\bar{1}$0] zone axis, the inset is Fast Fourier transform (FFT) pattern. **c**–**f** Enlargement of HRTEM images in (**b**) marked by (**c**–**f**), respectively. **g**–**i** HRTEM images showing high density of dislocations, nano-twins, and multiple stacking faults (MSFs) in NC grains. **j** HRTEM image showing the intersected SFs. The insets in (**h**–**j**) are the corresponding FFT patterns.

Microstructure evolution

Figure 3a shows the BF-STEM image before micropillar compression, which reveals that the 16 vol% DMGr/Cu-60 h exhibits a fine NC-grained structure with an average diameter of 19 nm and an average nanoparticle size of 3.77 nm (Supplementary Fig. 14). Selected-area electron diffraction (SAED) pattern (inset in Fig. 3a) indicates that a significant fraction of grains was highly misoriented. High-resolution TEM (HRTEM) image of a grain with DMGr distributing along GBs shows that there were several dislocations within the grain interior (Fig. 3b). Furthermore, the enlargement of HRTEM images (Fig. 3c–f) presents the distinct levels of lattice expansion in different regions within the grain interior due to the presence of C atoms in Cu lattice, such as 0.2216 nm for (111) and 0.231 nm for (11$\bar{1}$) plane in the d region. Corresponding GPA maps of regions d and e were displayed in Supplementary Fig. 15, which indicates that the strain distribution is also fluctuating and more significant with increasing volume fraction of DMGr compared with 1.5 vol% DMGr/Cu-30 h.

The post-mortem TEM characterizations were conducted on the deformed micropillar to reveal the dislocation configurations (Fig. 3g–j). HRTEM observations (Fig. 3g) show that more dislocations in different slip systems were pile-up in the grain interior, resulting in the formation of several Lomer-Cottrell (L-C) locks (white dashed circle), which is in sharp contrast to the belief that dislocations cannot be stored in nanograins during plastic deformation[13,49,50]. Besides, high density of nano-twins, multiple stacked faults (MSFs), and intersected SFs were also observed in nanograins (Fig. 3h–j), formed via Shockley partial dislocation emanating from DMGr/Cu interface[51,52]. Such dislocation configurations with high density can provide the dislocation obstacles responsible for the unusual strain hardening capacity and high strength. Furtherly, BF-STEM and HAADF-STEM morphologies, as presented in Fig. 4a–d and Supplementary Fig. 16, reveal the changes of structures before and after micropillar compression. Apart from the observed high-density dislocation configurations (Supplementary Fig. 17), another important feature is the interlayer sliding of DMGr during compression, which can be anticipated that their interlayer sliding can mediate plastic deformation and enhance plasticity[33]. The deformation mechanisms of our composite were furtherly investigated by in situ TEM compression (Fig. 4f–j and Supplementary Movie 2). Figure 4f–j displays the frame-by-frame analysis for the evolution of interlayer sliding of DMGr and lattice defects during compression. Upon compression, interlayer sliding of DMGr and dislocation motion were observed, and it should be noted that dislocation annihilation occurs subsequently due to the interlayer sliding of DMGr, as indicated by the change in relative contrast. However, it was quite difficult to catch the individual events of generation and annihilation on the movie. After the interlayer sliding of DMGr was completed, the high intrinsic strength of DMGr ultimately resulted in dislocation accumulations and activation of nano-twins within the nanograin interior. Therefore, the observed interlayer sliding of DMGr and dislocation configurations are believed to be closely linked with the high strength and superior plasticity in our composite. In contrast, the microstructure evolution of NC Cu before and after micropillar compression (Supplementary Fig. 18) indicates unremarkable dislocation accumulations in nanograins, exhibiting significant differences in deformation mechanisms between DMGr/Cu and NC Cu (Supplementary Note 3).

The schematic map is presented in Fig. 4e to depict the differences of structure evolution in our composite compared with polycrystalline metals. Introducing numerous GBs to refine grain sizes to the nanoscale has been proven efficient in strengthening materials by orders of magnitude. Nevertheless, the occurrence of grain rotation or GBs sliding results in a decrease of strength. In our composites, the interlayer sliding of DMGr gradually sets in as the stress builds up due to weak van der Waals forces between multilayers (Supplementary Fig. 21). Meanwhile, the presence of sp^3 covalent bonding can effectively avoid premature failure caused by van der Waals forces. Friction force measurements using atomic force microscope (AFM) and Molecular dynamics (MD) simulations (Supplementary Note 4) reveal that sp^3 bonding endows with DMGr (198.2 MPa) higher shear strength compared with GO (145.2 MPa). Moreover, uniformly and densely

https://doi.org/10.1038/s41467-025-62184-0

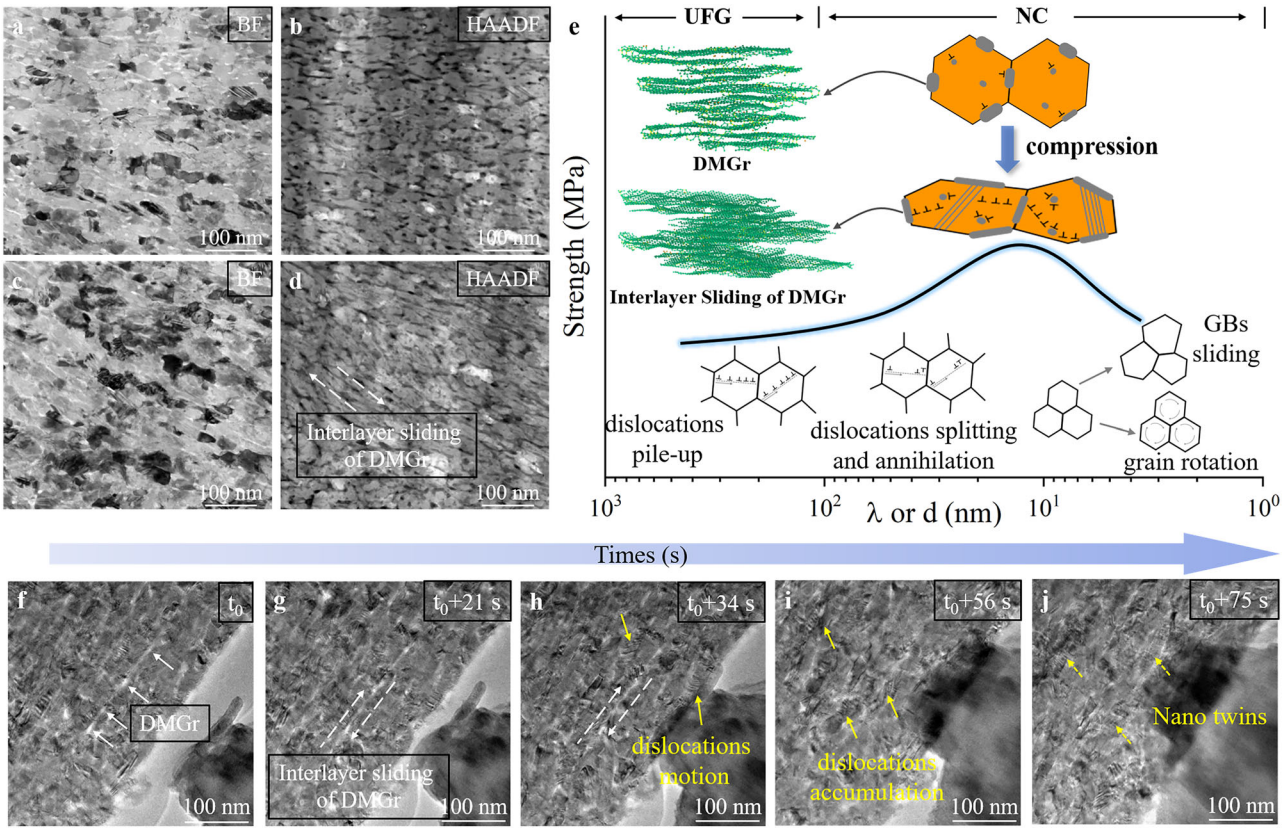

Fig. 4 | Transmission electron microscopy (TEM) microstructure of 16 vol% DMGr/Cu-60 h before and after micropillar compression. a, **b** BF-STEM and HAADF-STEM images before compression. **c**, **d** BF-STEM and HAADF-STEM images after compression. **e** Schematic map showing strengthening mechanisms in UFG, NC grains, and our composite. The curve represents the variation of strength with grain size, where the decrease in strength is caused by grain rotation or GBs sliding. In addition, the inset at the top displays structure changes and DMGr sliding in our composite during compression. **f**–**j** TEM images under in situ compression at different instantaneous times.

dispersed DMGr and associated Cu lattice strain caused by strong interactions between DMGr and matrix can effectively promote dislocation accumulation and storage within nanograins. Ultimately, a high density of dislocation configurations and interlayer sliding of DMGr can lead to high strength and superior plasticity in our composite.

Differential scanning calorimetry (DSC) analysis (Supplementary Fig. 24), in situ high-temperature XRD experiments (Supplementary Fig. 25), and microstructure evolutions (Supplementary Fig. 26) display that DMGr/Cu composites exhibit better thermal stability than NC Cu. The lattice parameter of pure copper gradually increased with elevating temperature and maintained almost the same slope during the heating and cooling processes (Supplementary Fig. 25c). The slight change of lattice parameter at the same temperature for heating and cooling stages indicated that high-energy ball milling introduced a small amount of lattice distortion in the matrix. In contrast, the lattice parameter of the DMGr/Cu sample did not begin to increase until 300 °C, and the slope was smoother during the whole heating compared with pure copper. Surprisingly, the slope of DMGr/Cu during the cooling process was similar to that of pure copper. Above all, it can be inferred that the change in lattice parameter of DMGr/Cu was significantly higher than that of pure copper at the same temperature during heating and cooling, which can be indicated that the presence of DMGr led to higher lattice strain. The nanoindentation results (Supplementary Fig. 25d) of 16 vol% DMGr/Cu-60 h annealed at different temperatures for 1 h displayed that the hardness began to decrease at 300 °C. An explanation of the observed behavior could be related with the hindrance of DMGr to GBs migration. Based on the microstructure evolutions of 16 vol% DMGr/Cu-60 h sample annealing at different temperatures, we can infer that DMGr can hinder the migration of GBs, inhibit grain coarsening, and thus contribute to better thermal stability of DMGr/Cu than NC Cu.

MD simulations

EELS and APT results (Fig. 1g, i and j) reveal that the addition of DMGr caused lattice expansion and lattice strain near the interface (Supplementary Figs. 9 and 15). In order to fully understand the effect of lattice strain on the mechanical properties in our composites, we adopted MD simulations to investigate the deformation behavior of DMGr/Cu composites under uniaxial compression with and without lattice expansion. Schematic of atomic configuration of simulated DMGr/Cu system is presented in Fig. 5a with the x, y, and z axes for $[1\bar{1}0]$, $[11\bar{2}]$, and [111], respectively, and lattice expansion was introduced by making some C atoms into matrix lattice (Supplementary Fig. 27). With applied straining, stress-strain curves (Fig. 5b) were obtained for DMGr/Cu composites with and without lattice expansion, where the composite with lattice strain exhibited higher stress compared without lattice strain, consisting with the evolution of lattice strain (Fig. 5c). In the presence of lattice strain, we believe that the movement of dislocations at the sites with strain requires higher shear stress to initiate, leading to a significant dislocation propagation at higher strain (Fig. 5f)[53]. Meanwhile, more slip systems will be activated to participate in the plastic deformation and further contribute to dislocation multiplication with a fast rate (Fig. 5d, e). The corresponding microstructure evolution of DMGr/Cu composites at strains of 15% and 45% with and without lattice expansion are displayed in Fig. 5g–j. In the absence of lattice strain (Fig. 5g), it can be

https://doi.org/10.1038/s41467-025-62184-0

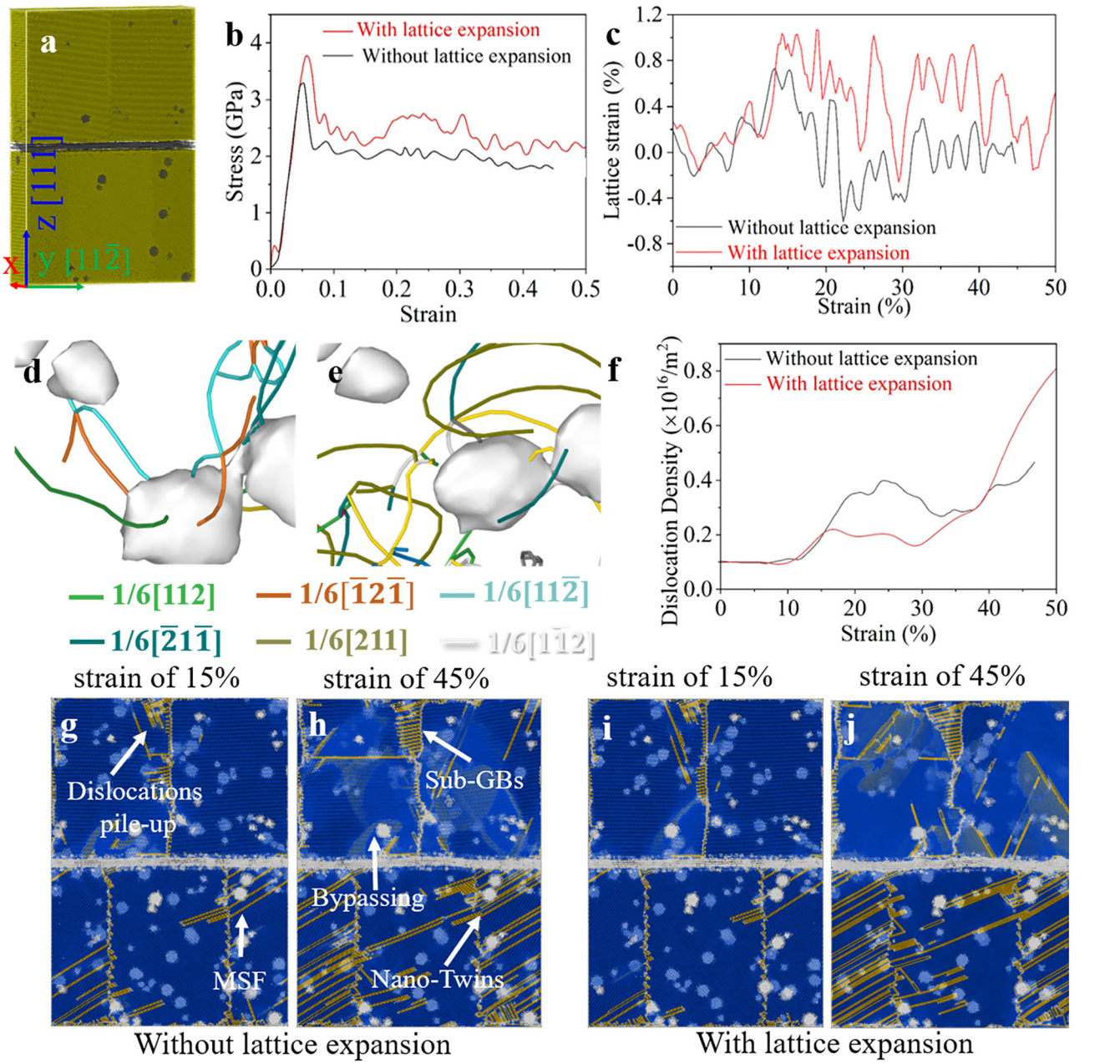

Fig. 5 | Molecular dynamics (MD) simulations for DMGr/Cu composites with and without lattice expansion. a Schematic of the atomic configuration for the simulated DMGr/Cu system. **b** Stress-strain curve. **c** Lattice strain with increasing strain. **d** The dislocation configuration in the composite without lattice expansion at a strain of 45%. **e** The dislocation configuration in the composite with lattice expansion at a strain of 45%, exhibiting that more slip systems participate in the plastic deformation. **f** The dislocation density with applied strain. Here, "with lattice expansion" represents 10% of three-layer C atoms are introduced into the matrix with a thickness of about 1 nm at the interface, and 10% of DMGr particles are introduced into the matrix around the particles within a range of about 0.5 nm. **g**, **h** Snaps of DMGr/Cu composite without lattice expansion at strain 15% and 45%. **i**, **j** Snaps of DMGr/Cu composite with lattice expansion at strain 15% and 45%.

seen that at a strain of 15%, dislocations pile-up occurred near the GBs, making it more prone to dislocation multiplication and improving strength. In addition, a Frank Reed (FR) dislocation source was generated on both the DMGr nanoparticle and DMGr layers and bypasses the DMGr nanoparticle. This is because the *z*-direction is perpendicular to the (111) crystal plane, and the slip of edge dislocations will be suppressed. And the dislocations naturally tended to through the FR dislocation source mechanism, and this phenomenon occurred multiple times during compression. MSFs were also observed by appearing three penetrating incomplete dislocations. High density of dislocations was formed as the strain increasing to 45% (Fig. 5h). In contrast, the density of dislocations was relatively low at small strain for composite with lattice strain (Fig. 5i). However, dislocations rapidly propagated and the ultimate dislocation density was significantly higher than the former at high strain conditions (Fig. 5j). Ultimately, dislocations can multiply and be activated in multiple slip systems in strain fields, improving the strength and plasticity of DMGr/Cu composite.

Discussion

High strain hardening capacity

In general, NC metals fabricated by SPD, such as high-pressure torsion (HPT) and equal channel angular pressing (ECAP), usually possess strength that can be several times higher than that of their coarse-

grained counterparts, but very low ductility[1,2]. Because conventional dislocation sources in the grain interior are no longer exist due to the small grain size (<100 nm) and GBs become the main dislocation sources[3,54,55]. Due to the abundant dislocation sources (GBs), dislocations are rapidly generated to decorate the grains and their boundaries, resulting in a high strain hardening rate in the early stages of plastic deformation[10]. The dislocations emitted from GBs glide across the grain interior and are highly likely to be adsorbed by GBs due to the small distance[56]. Further, these adsorbed dislocations may annihilate with other dislocations with the opposite Burgers vectors. The adsorption and annihilation processes of dislocations are both rapid because their rates are controlled by GB diffusion, which is much faster than overall diffusion[1]. Due to the high annihilation rate, dislocations cannot effectively accumulate in the grain interior, resulting in immediate plastic instability after yielding[7]. The process of work hardening can be understood at the microstructural level through the interactions of dislocations, which is very limited in nanograins[57]. This is the typical characteristic of plastic deformation in NC metals, where dislocations are quickly emitted and annihilated at GBs during plastic deformation. The above discussed phenomenon has been observed in the nanostructured ECAP-Ti and ECAP-Cu, and it was found that there are mostly free of dislocations in UFG and nanograins, which is the primary reason contributing to low work hardening rate and low ductility[10,58].

In our NC composite, dislocations were emitted from GBs and glided across the grain interior, while they were not quickly adsorbed and annihilated by GBs like conventional nanograins under plastic deformation[2]. The presence of DMGr and lattice strain near DMGr/Cu interfaces (Supplementary Figs. 9 and 15) impeded the movement of dislocations (typical feature being wavy dislocation lines), leading to the entanglement and interaction of dislocations (Fig. 3g–j). The accumulation of dislocations elevated the stress required to overcome further plastic deformation[59]. In addition to hindering dislocation movement, the DMGr and corresponding lattice strain can also act as dislocation sources to generate dislocations, enabling the activation of dislocations in multi slip systems and further promoting the accumulation of dislocations (Fig. 5). Furthermore, the reactions of dislocations can form L-C locks (Fig. 3g), because the high density of dislocations on different slip systems are prone for the formation of L-C locks[13,51]. Recent works hve demonstrated that L-C locks play a critical role in strain hardening, which derive their effectiveness from the capacity to accumulate dislocations[49,50], thus we believe that L-C locks are effective in producing strain hardening in our composite. In addition, MSFs and nanotwins, formed via Shockley partial dislocation emitted from the DMGr/Cu interface, were also observed in the post-mortem TEM morphologies (Fig. 3h, i), which can provide room for dislocation accumulation and interactions[60]. When gliding dislocations meet with nanotwins, they can pile up at the twin boundaries and interact with twin boundaries in multiple ways[23,61]. The observed nanotwins appear to be messy, as a result of contain dislocations at twin boundaries and interior. The interactions between dislocations and twin boundaries, making the twin boundaries effective sites for dislocation accumulations, are predicted to be effective to promote strain hardening and generate excellent plasticity[62]. The MSFs can interact with dislocations in a similar way with twin boundaries, promoting dislocation storage and increasing strain hardening. And the intersected SFs introduced during straining may be extra dislocation sources, hindering further dislocation movement. The formed new interfaces and dislocation entanglement are expected to promote strain hardening (Fig. 3j). The above dislocation behaviors in this work are of great significance, because accumulation and storage of dislocations in NC grains are usually very limited[1]. The addition of DMGr and correspondingly generated lattice strain near the interface caused by strong interactions between DMGr and matrix made dislocation motion sluggish in nanograins, promoting the interactions and accumulation of dislocations, contributing to superior strain hardening capacity (Fig. 2d, e). Therefore, the high-density dislocations coupled with nanotwins and MSFs jointly improve the storage of dislocations in nanograins and contribute to ultra-high strength, enhanced hardening capacity, and superior plasticity. The contribution order of corresponding strengthening mechanisms in our DMGr/Cu composite is Hall-Petch related strengthening (149.3 MPa), dislocation strengthening (117.8 MPa), and load transfer strengthening (72.9 MPa, Supplementary Note 5).

Interlayer sliding of DMGr upon compression

GBs sliding is one of the dominant deformation mechanisms in NC metals during the plastic deformation, which can improve the plasticity[63,64]. Gr not only has excellent mechanical and physical properties, but also exhibits significant self-lubricating effects due to the weak van der Waals forces between Gr interlayers[65]. However, due to the poor wettability between Gr and Cu, there exists a competitive relationship between Gr strengthening, Gr lubricating, and interface delamination. The weakly bonded Gr/Cu interface are prone to cause interface delamination and eventually leads to catastrophic failure[65]. In this work, uniformly and densely dispersed DMGr with sp^2-sp^3 hybridization were obtained by PABM. The strong interactions between DMGr and the matrix induce lattice expansion and generate lattice strain, promoting the interactions and storage of dislocations within nanograins. In addition to effectively block dislocation motions of DMGr due to high strength, the presence of small amount sp^3 covalent bonding at interlayer make these DMGr can assist plastic deformation through interlayer sliding much stronger than the van der Waals forces, avoiding premature failure, which were observed in ex-situ and in situ characterizations (Fig. 4). We believed that the interlayer sliding of DMGr can be similar to the GB sliding mechanism in assisting plastic deformation, leading to higher plasticity. Moreover, the gliding dislocations that are piled up at the DMGr-Cu interface may escape to the free surface through interfacial sliding to further accommodate the plastic deformation of the composite[32]. Consequently, the interfacial nanostructuring design proposed here generated DMGr with mixed sp^2-sp^3 hybridized carbon atoms, which can not only improve the mechanical properties by impeding dislocation motion but also mediate plastic deformation and thus enhance plasticity via interlayer sliding of DMGr.

In summary, we propose an interface nanostructuring design via PABM to fabricate DMGr/Cu composites, achieving uniformly and densely dispersed DMGr with mixed sp^2-sp^3 hybridized carbon atoms. The synthesized NC DMGr/Cu composite exhibited a nanoindentation hardness of 6.2 GPa and a compressive strength of 1.56 GPa, as well as a plastic strain of exceeding 0.6, suggesting a superior combination of strength and plasticity. Ex-situ and in situ TEM characterizations revealed that the high-density dislocation configurations in nanograins interior, including high-density dislocations, nanotwins, and MSFs, induced by DMGr and associated lattice strain along with interlayer sliding of DMGr contributed to ultra-high strength and superior plasticity. This strategy by manipulating interface nanostructuring design, provides a promising approach to manufacturing ultra-strong and plastic NC metals for structural applications.

Methods

Materials preparation

Spherical copper powders (Shanghai Buwei Applied Materials Technology Co., Ltd, d_{10}, d_{50} and d_{90} = 0.463, 0.674 and 0.954 μm, respectively) and graphene oxide (GO) (Nanjing XFNano Material Tech Co., Ltd) were annealed at 300 °C for 2 h under H_2/Ar (5 vol.% H_2) atmosphere to remove the surface impurities and oxides. Then, copper powders, GO with different volume fractions (0, 1.5, 3, 5, 8, and 16 vol%), and hard alloy balls were loaded into a cylindrical stainless-steel ball milling tank with a Cu-powder-to-milling-ball mass ratio of

approximately 1:10. The tank was vacuumed and filled with high-purity argon gas. The DMGr/Cu composites were in situ synthesized by PABM for different times (15 h, 20 h, 30 h, 45 h, 60 h, 80 h, and 100 h) under a speed of 1200 rpm and frequency of 10 kHz. The samples to investigate thermal stability were performed by annealing at different temperatures (200, 300, 400, and 450 °C) for 1 h in a tube furnace under H_2/Ar atmosphere.

Microstructure characterizations

The surface morphology and energy dispersive spectroscopy (EDS) analysis of flakes were performed on a RISE-MAGNA scanning electron microscope (SEM). A high-resolution X-ray photoelectron spectroscopy (XPS, Escalab Qxi) was utilized to investigate surface charge properties of the composite. Raman spectroscopy (Reinishow inVia Qontor), using an excitation wavelength of 532 nm under a 200 s acquisition time, was used to characterize the changes in various peaks of RGO before and after ball milling. XRD tests were conducted on a D8 ADVANCE Da Vinci (Cu Kα) with a 2θ range of 15–85°, step size of 0.02°, and a scan speed of 10°/min at room temperature to analyze crystallographic orientations. DSC analysis was carried out by a DSC 404 F3 in the temperature range of 100 °C–700 °C with the heating rate of 10 °C/min. In situ high-temperature XRD measurements were performed on an ARL Equinox 3500 with a ramping rate of 20 °C/min. The samples for TEM analysis and in situ micropillar/TEM compression tests were prepared via focus ion beam (FIB) milling on a FEI helios 5ux FIB. Furtherly, the specimens were milled by Fischione 1040 NanoMill to remove the surface amorphous layer and Ga^+ implantation with a milling voltage of 500 eV and milling current of 100 μA. Transmission electron microscopy (TEM) characterizations and EDS mapping were performed on a FEI Talos F200X equipped with a Super-X EDS system with an accelerating voltage of 200 kV. The characterizations of atom mapping using the advanced iDPC-STEM technique and (electron energy loss spectra) EELS analysis were carried out on an aberration-corrected scanning transmission electron microscope (Spectra 300, FEI). Precession electron diffraction (PED, NanoMEGAS) measurements before and after micropillar compression were conducted on a Spectra 300 equipped with an ASTAR system, and a precession angle of 0.6° with a step size of 2 nm.

Atom probe tomography (APT). APT analysis was performed on a local electrode atom probe (CAMECA LEAP4000X Si) to investigate the three-dimensional elemental distribution at the atomic scale. Needle-shaped tips for APT analysis were produced by a FIB lift-out method using a dual Focused Ion Beam (FIB)-SEM system (ZEISS Auriga Crossbeam). The final-step milling of each tip was conducted at a very low accelerating voltage of 5 kV and a beam current of 5 pA to minimize Ga^+ implantation. APT experiments were run at a specimen temperature of 40 K, under a UV laser pulsing, at a repetition rate of 200 kHz, a pulsing laser energy of 40 pJ, and a target evaporation rate of 0.5% per pulse under an ultrahigh vacuum of 5.0×10^{-11} Torr. APT dataset reconstruction and quantitative analysis were conducted with the commercial software CAMECA AP Suite version 6.3.

Mechanical testing

The hardness of DMGr/Cu composites were measured by nanoindentation test (Nano Indenter G200) with a maximum depth of 150 nm at room temperature. In situ micropillar compression tests were conducted by a 5-μm diamond flat punch equipped on a FEI Helios 600 FIB, utilizing displacement-controlled mode at an approximate rate of 2 nm/s. The diameter of the micropillar was 2 μm with aspect ratios (height/diameter) of 2:1-3:1. In situ TEM compression were performed on Cs-TEM (JEOL Grand ARM300) using a Hysitron PI 95 Picoindenter system equipped with a flat diamond tip. Displacement-controlled mode at a displacement rate of 0.25 nm/s was operated with TriboScan software suite. The in situ videos were obtained using a Gatan OneView camera with 1 k resolution at a speed of 25 frames/s.

Friction Force Measurements using AFM

Friction force measurements were conducted by atomic force microscope (AFM, Dimension XR, Bruker) in air at room temperature. Standard force modulation silicon probe (OMCL-AC240TS-R3) with a resonant frequency of 70 kHz, nominal spring constant of 1.7 N/m, and tip radius of ~ 7 nm was used. Under lateral force scanning mode with a canning rate of 1 Hz, trace/retrace *vs* distance curves were recorded over areas of 500 nm × 500 nm consisting of 256 lines. The friction force was estimated by subtracting and halving the mean values of trace-retrace signals.

First principles calculations

First-principles calculations based on density functional theory (DFT) were performed in the Vienna Ab initio Simulation Package (VASP) software. The exchange correlation between electrons is described using the Perdew-Burke-Ernzerhof (PBE) form of generalized gradient approximation (GGA) following the criteria[66,67]: cutoff energy of 500 eV, energy convergence accuracy of 1×10^{-6} eV, force error less than 0.01 eV/Å acting on the atom, and value of $2 \times 2 \times 1$ for the Brillouin zone k-point. By thoroughly optimizing the geometry of two initial models and performing energy calculations based on displacement path interpolation points, atomic force data of initial and displaced structures were extracted to elucidate the essential cause of lattice expansion.

Molecular dynamic simulations

Molecular dynamics (MD) simulations using Large-scale Atomic Molecular Massively Parallel Simulator (LAMMPS) were performed to investigate the interactions between DMGr and dislocations. And simulation configurations were visualized by the Open Visualization Tool (OVITO). During the simulation process, embedded atom method (EAM)[68] and Modified embedded-atom method (MEAM)[69] potentials were used for Cu-Cu and C-C atomic interactions, respectively, and the interaction between Cu-C atoms was described by Lennard-Jones potential (L-J) potential[70,71]. The entire simulation phase was conducted under periodic boundary conditions and NPT ensemble, with a time step of 1 fs. The initial model relaxed for 100 ps at 300 K and ambient pressure to ensure that the model reached a stress equilibrium state. To carry out compression simulations of DMGr/Cu composite, a $10 \times 40 \times 60$ nm model (2001100 atoms) was constructed for MD simulation, including four grains with a single grain size of $10 \times 20 \times 30$ nm. The corresponding crystal orientations on the x, y, and z axes were $[1\bar{1}0]$, $[11\bar{2}]$, and [111], respectively. The intergranular DMGr contains three layers of graphene, and the intragranular DMGr particles have a diameter of 1-2 nm. In order to introduce lattice expansion, about 10% of three-layer C atoms were introduced into the matrix with a distance of about 1 nm at the interface, and 10% of DMGr particles were introduced into the matrix around the particles within a range of about 0.5 nm. The positions were randomly distributed, and all C atoms entering the copper matrix were located between the Cu lattice.

Data availability

All data are available in the manuscript and the Supplementary Information. Source data are provided in this paper.

References

1. Ovid'ko, I. A., Valiev, R. Z. & Zhu, Y. T. Review on superior strength and enhanced ductility of metallic nanomaterials. *Prog. Mater. Sci.* **94**, 462–540 (2018).
2. Zhu, Y. T. & Wu, X. L. Heterostructured materials. *Prog. Mater. Sci.* **131**, 101019 (2023).

3. Dao, M., Lu, L., Asaro, R. J., Hosson, J. T. M. D. & Ma, E. Toward a quantitative understanding of mechanical behavior of nanocrystalline metals. *Acta Mater.* **55**, 4041–4065 (2007).
4. Wang, Y. M., Chen, M. W., Zhou, F. H. & Ma, E. High tensile ductility in a nanostructured metal. *Nature* **419**, 912–915 (2002).
5. Lu, K., Lu, L. & Suresh, S. Strengthening materials by engineering coherent internal boundaries at the nanoscale. *Science* **324**, 349–352 (2009).
6. Wang, Y. M. et al. Microsample tensile testing of nanocrystalline copper. *Scripta Mater.* **48**, 1581–1586 (2003).
7. Ma, E. Instabilities and ductility of nanocrystalline and ultrafine-grained metals. *Scripta Mater.* **49**, 663–668 (2003).
8. Wang, Y. M. & Ma, E. Enhanced tensile ductility and toughness in nanostructured Cu. *Appl. Phys. Lett.* **80**, 2395–2397 (2002).
9. Zhang, Y., Tao, N. R. & Lu, K. Mechanical properties and rolling behaviors of nano-grained copper with embedded nano-twin bundles. *Acta Mater.* **56**, 2429–2440 (2008).
10. Wang, Y. M. & Ma, E. Three strategies to achieve uniform tensile deformation in a nanostructured metal. *Acta Mater.* **52**, 1699–1709 (2004).
11. Li, Z. et al. *Nat. Commun.* **13**, 5581 (2022).
12. Duan, F. H. et al. An order-disorder core-shell strategy for enhanced work-hardening capability and ductility in nanostructured alloys. *Nat. Commun.* **15**, 6832 (2024).
13. Wu, X. L., Zhu, Y. T., Wei, Y. G. & Wei, Q. Strong Strain Hardening in Nanocrystalline Nickel. *Phys. Rev. Lett.* **103**, 205504 (2009).
14. Ma, E. & Wang, Y. M. Strain hardening and large tensile elongation in ultrahigh-strength nano-twinned copper. *Appl. Phys. Lett.* **85**, 4932–4934 (2004).
15. Luis, A., Ruiz, Z., Stukowski, A., Oppelstrup, T. & Bulatov, V. V. Probing the limits of metal plasticity with molecular dynamics simulations. *Nature* **550**, 492–495 (2017).
16. Wu, X. L. et al. Heterogeneous lamella structure unites ultrafine-grain strength with coarse-grain ductility. *PNAS* **112**, 14501–14505 (2015).
17. Li, X. Y., Lu, L., Li, J. G., Zhang, X. & Gao, H. J. Mechanical properties and deformation mechanisms of gradient nanostructured metals and alloys. *Nat. Rev. Mater.* **5**, 706–723 (2020).
18. Zhu, Y. T. & Wu, X. L. Perspective on heterogeneous deformation induced (HDI) hardening and back stress. *Mater. Res. Lett.* **7**, 393–398 (2019).
19. Cheng, Z., Zhou, H.F., Lu, Q.H., Gao, H.J. & Lu, L. Extra strengthening and work hardening in gradient nanotwinned metals. *Science* **362**, https://doi.org/10.1126/science.aau1925 (2018).
20. Wei, Y. J. et al. Evading the strength-ductility trade-off dilemma in steel through gradient hierarchical nanotwins. *Nat. Commun.* **5**, 3580 (2014).
21. Gu, J. L., Duan, F. H., Liu, S. D., Cha, W. H. & Lu, J. Phase engineering of nanostructural metallic materials: Classification, structures, and applications. *Chem. Rev.* **124**, 1247–1287 (2024).
22. Lu, L., Shen, Y. F., Chen, X. H., Qian, L. H. & Lu, K. Ultrahigh strength and high electrical conductivity in copper. *Science* **304**, 422–426 (2004).
23. Lu, L., Chen, X., Huang, X. & Lu, K. Revealing the maximum strength in nanotwinned Copper. *Science* **323**, 607–610 (2009).
24. Peng, S. Y., Wei, Y. J. & Gao, H. J. Nanoscale precipitates as sustainable dislocation sources for enhanced ductility and high strength. *PNAS* **117**, 5204–5209 (2020).
25. Rong, X. D. et al. Towards the work hardening and strain delocalization achieved via in situ intragranular reinforcement in Al-CuO composite. *Acta Mater.* **256**, 119110 (2023).
26. Khalajhedayati, A., Pan, Z. L. & Rupert, T. J. Manipulating the interfacial structure of nanomaterials to achieve a unique combination of strength and ductility. *Nat. Commun.* **7**, 10802 (2016).
27. Ming, K. S. et al. Enhancing strength and ductility via crystalline-amorphous nanoarchitectures in TiZr-based alloys. *Sci. Adv.* **8**, 2884 (2022).
28. Gao, B. et al. Ultrastrong low-carbon nanosteel produced by heterostructure and interstitial mediated warm rolling. *Sci. Adv.* **6**, eaba8169 (2020).
29. Liu, C. et al. Near-theoretical strength and deformation stabilization achieved via grain boundary segregation and nano-clustering of solutes. *Nat. Commun.* **15**, 9283 (2024).
30. Lv, H. et al. Bamboo-like dual-phase nanostructured copper composite strengthened by amorphous boron framework. *Nat. Commun.* **14**, 4836 (2023).
31. Wu, G., Chan, K. C., Zhu, L. L., Sun, L. G. & Lu, J. Dual-phase nanostructuring as a route to high-strength magnesium alloys. *Nature* **545**, 80–83 (2017).
32. Kim, Y. et al. Strengthening effect of single-atomic-layer graphene in metal–graphene nanolayered composites. *Nat. Commun.* **4**, 2114 (2013).
33. Zhang, X. H. et al. Multilayer graphene interface enabled ultrahigh extensibility for high performance bulk nanostructured copper. *Acta Mater.* **267**, 119710 (2024).
34. Chen, F. Y. et al. Effects of graphene content on the microstructure and properties of copper matrix composites. *Carbon* **96**, 836–842 (2016).
35. Robertson, J. Diamond-like amorphous carbon. *Mater. Sci. Eng. R Rep.* **37**, 129–281 (2002).
36. Hu, M. et al. Compressed glassy carbon: An ultrastrong and elastic interpenetrating graphene network. *Sci. Adv.* **3**, e1603213 (2017).
37. Li, Z. H. et al. Ultrastrong conductive in situ composite composed of nanodiamond incoherently embedded in disordered multilayer graphene. *Nat. Mater.* **22**, 42–49 (2023).
38. Liu, X. R., Liu, Y. B., Ran, X., An, J. & Cao, Z. Y. Fabrication of the supersaturated solid solution of carbon in copper by mechanical alloying. *Mater. Character.* **58**, 504–508 (2007).
39. Marques, M. T., Correia, J. B. & Conde, O. Carbon solubility in nanostructured copper. *Scripta Mater.* **50**, 963–967 (2004).
40. Chen, Z. et al. Electron ptychography achieves atomic-resolution limits set by lattice vibrations. *Science* **372**, 826–831 (2021).
41. Ding, Q. Q. et al. Tuning element distribution, structure and properties by composition in high-entropy alloys. *Nature* **574**, 223–227 (2019).
42. Jiang, S. et al. Interstitial carbon induced FCC-Ti exhibiting ultrahigh strength in a $Ti_{37}Nb_{28}Mo_{28}$-C_7 complex concentrated alloy. *Acta Mater.* **203**, 116456 (2021).
43. Lu, Y. G. et al. Direct visualization of boron dopant distribution and coordination in individual chemical vapor deposition nanocrystalline B-doped diamond grains. *Appl. Phys. Lett.* **101**, 041907 (2012).
44. Ferrari, A. C. & Robertson, J. Raman spectroscopy of amorphous, nanostructured, diamondlike carbon, and nanodiamond. *Philos. Trans. R. Soc. A* **362**, 2477–2512 (2004).
45. Cheng, S. et al. Tensile properties of in situ consolidated nanocrystalline Cu. *Acta Mater.* **53**, 1521–1533 (2005).
46. Zhang, J. Y. et al. Length scale-dependent deformation behavior of nanolayered Cu/Zr micropillars. *Acta Mater.* **60**, 1610–1622 (2012).
47. Li, H. Q. et al. Strong and ductile nanostructured Cu-carbon nanotube composite. *Appl. Phys. Lett.* **95**, 071907 (2009).
48. Zhang, J. Y., Li, J., Liang, X. Q., Liu, G. & Sun, J. Achieving optimum mechanical performance in metallic nanolayered Cu/X (X 5 Zr, Cr) micropillars. *Sci. Rep.* **4**, 4205 (2014).
49. Li, H. et al. Uniting tensile ductility with ultrahigh strength via composition undulation. *Nature* **604**, 273–279 (2022).
50. Fan, L. et al. Ultrahigh strength and ductility in newly developed materials with coherent nanolamellar architectures. *Nat. Commun.* **11**, 6240 (2020).

51. Liao, X. Z. et al. Deformation twinning in nanocrystalline copper at room temperature and low strain rate. *Appl. Phys. Lett.* **84**, 592–594 (2004).
52. Peng, Y. F., Luo, G. H., Hu, Y. X. & Xiong, D. B. Extreme strain rate deformation of nacre-inspired graphene/copper nanocomposites under laser-induced hypersonic micro-projectile impact. *Compos. Part B* **235**, 109763 (2022).
53. Lia, J. et al. Heterogeneous lattice strain strengthening in severely distorted crystalline solids. *PNAS* **119**, e2200607119 (2022).
54. Ovid'ko, I. A., Sheinerman, A. G. & Valiev, R. Z. Dislocation emission from deformation-distorted grain boundaries in ultrafine-grained materials. *Scripta Mater.* **76**, 45–48 (2014).
55. Li, X. C. et al. Direct observation of the grain boundaries acting as dislocation sources in nanocrystalline platinum. *Mater. Character.* **181**, 111493 (2021).
56. Aragon, N. K., Gravell, J. D. & Ryu, I. Dislocation interactions at the grain boundary in FCC bicrystals: An atomistically-informed dislocation dynamics study. *Acta Mater.* **223**, 117455 (2022).
57. Hughes, D. A. & Hansen, N. The microstructural origin of work hardening stages. *Acta Mater.* **148**, 373–383 (2018).
58. Jia, D. et al. Deformation behavior and plastic instabilities of ultrafine-grained titanium. *Appl. Phys. Lett.* **79**, 611–613 (2001).
59. Zhao, Y. H. et al. Dislocation motion in plastic deformation of nano polycrystalline metal materials: a phase field crystal method study. *Adv. Compos. Hybrid Mater.* **5**, 2546–2556 (2022).
60. Zhu, Y. T. et al. Dislocation–twin interactions in nanocrystalline fcc metals. *Acta Mater.* **59**, 812–821 (2011).
61. Cheng, Z., Zhou, H. F., Lu, Q. H., Gao, H. J. & Lu, L. Extra strengthening and work hardening in gradient nanotwinned metals. *Science* **362**, eaau1925 (2018).
62. Zhang, Z. J. et al. Dislocation mechanisms and 3D twin architectures generate exceptional strength-ductility-toughness combination in CrCoNi medium-entropy alloy. *Nat. Commun.* **8**, 14390 (2017).
63. Schiøtz, J. & Jacobsen, K. W. A maximum in the strength of nanocrystalline copper. *Science* **301**, 1357–1359 (2003).
64. Wang, L. H. et al. Tracking the sliding of grain boundaries at the atomic scale. *Science* **375**, 1261–1265 (2022).
65. Lin, G. Y. et al. Remarkable anisotropic wear resistance with 100-fold discrepancy in a copper matrix laminated composite with only 0.2 vol% graphene. *Acta Mater.* **215**, 117092 (2021).
66. Payne, M. C., Teter, M. P., Allan, D. C., Arias, T. & Joannopoulos, A. J. Iterative minimization techniques for ab initio total-energy calculations: molecular dynamics and conjugate gradients. *Rev. Mod. Phys.* **64**, 1045 (1992).
67. Perdew, J. P., Burke, K. & Ernzerhof, M. Generalized gradient approximation made simple. *Phys. Rev. Lett.* **77**, 3865 (1996).
68. Mishin, Y., Mehl, M., Papaconstantopoulos, D., Voter, A. F. & Kress, J. Structural stability and lattice defects in copper: Ab initio, tight-binding, and embedded-atom calculations. *Phys. Rev. B* **63**, 224106 (2001).
69. Lee, B. J. & Lee, J. W. A modified embedded atom method interatomic potential for carbon. *Calphad* **29**, 7–16 (2005).
70. Piątek, A., Nowak, R. & Gburski, Z. A Titanium-decorated fullerene cluster-a molecular dynamics simulation. *Solid State Phenom.* **140**, 109–116 (2008).
71. Rappe, A.K., Casewit, C.J., Colwell, K.S., Goddard III, W.A. & Skiff, W.M. UFF, A full periodic table force field for molecular mechanics and dynamics simulations. *J. Am. Chem. Soc.* **114**, 10024–10035 (1992).

Acknowledgements

This work was supported by the National Science Foundation of China (NSFC Nos. 52271134, 51971131), Shanghai Municipal Commission of Science and Technology (No. 21TQ1400215, 22DZ1101400), and Shanghai Jiao Tong University 2030 Initiative. The authors would like to thank Dr. Zhongxin Zhao and Dr. Fu Chen from Shanghai Jiao Tong University for their sample preparation and characterization.

Author contributions

Y.G.: Formal analysis, Writing-original draft, Methodology. D.X.: Conceptualization, Formal analysis, Writing-original draft, Project administration. D.Z.: Project administration. X.Z., L.Z. and Z.L.: Formal analysis. Y.Z.: In situ TEM compression experiments. R.Q. and X.L.: Analysis of in situ TEM compression data. Z.W. and G.S.: APT experiments and analysis. All the authors contributed to the final manuscript.

Competing interests

The authors declare no competing interests.

Additional information

Supplementary information The online version contains supplementary material available at https://doi.org/10.1038/s41467-025-62184-0.

Correspondence and requests for materials should be addressed to Ding-Bang Xiong.

Peer review information *Nature Communications* thanks Goknur Buke and the other anonymous reviewer(s) for their contribution to the peer review of this work. A peer review file is available.